Observation of crack initiation zone in brick masonry couplets under compression using X-ray microfocus computed tomography and digital image correlation

Shetty, Naveen; Livitsanos, Georgios; Verstrynge, Els; Aggelis, Dimitrios G.; Hemelrijck, Danny Van; Balen, Koen Van; Wevers, Martine

Published in:
International journal of masonry research and innovation

DOI:
10.1504/IJMRI.2020.111800

Publication date:
2020

License:
Unspecified

Document Version:
Accepted author manuscript

Observation of crack initiation zone in brick masonry couplets under compression using X-ray microfocus computed tomography and digital image correlation

Naveen Shetty*

Building Materials and Building Technology Division,
Department of Civil Engineering,
KU Leuven, Kasteelpark Arenberg 40,
3001 Heverlee, Belgium
Email: naveen.shetty@kuleuven.be
*Corresponding author

Georgios Livitsanos

Department of Mechanics of Materials and Constructions,
Vrije Universiteit Brussels,
Pleinlaan 2, 1050 Elsene, Brussels, Belgium
Email: georgios.livitsanos@vub.ac.be

Els Verstrynge

Building Materials and Building Technology Division,
Department of Civil Engineering,
KU Leuven, Kasteelpark Arenberg 40,
3001 Heverlee, Belgium
Email: els.verstrynge@kuleuven.be

Dimitrios G. Aggelis and
Danny Van Hemelrijck

Department of Mechanics of Materials and Constructions,
Vrije Universiteit Brussels,
Pleinlaan 2, 1050 Elsene, Brussels, Belgium
Email: daggelis@vub.ac.be
Email: dvhemelr@vub.ac.be

Koen Van Balen

Building Materials and Building Technology Division,
Department of Civil Engineering,
KU Leuven, Kasteelpark Arenberg 40,
3001 Heverlee, Belgium
Email: koenraad.vanbalen@kuleuven.be

Martine Wevers

Department of Materials Engineering,
KU Leuven, Kasteelpark Arenberg 44,
3001 Heverlee, Belgium
Email: martine.wevers@kuleuven.be

Abstract: The constituent materials of masonry include different brick and mortar types with various properties. The difference in the stiffness properties of these materials influence the observed failure modes under compression. The general theory of the failure mechanisms in brick masonry under compressive loading relies on the difference between the relative elastic modulus of brick and mortar. The aim of this paper is to visually examine the above theory about the behaviour of masonry under compression using a high-resolution X-ray micro-CT scanner. Additionally, full-scale couplets have been tested under compression with the application of stereo-vision digital image correlation (DIC). The failure progression in masonry which evolves from the initiation of micro cracks, over the propagation into macro cracks has been clearly evidenced. Overall, the results from DIC positively confirm the observation from X-ray micro-CT.

Keywords: masonry; compression; failure mechanisms; X-ray computed tomography; digital image correlation; DIC.

Reference to this paper should be made as follows: Shetty, N., Livitsanos, G., Verstrynge, E., Aggelis, D.G., Van Hemelrijck, D., Van Balen, K. and Wevers, M. (xxxx) 'Observation of crack initiation zone in brick masonry couplets under compression using X-ray microfocus computed tomography and digital image correlation', *Int. J. Masonry Research and Innovation*, Vol. X, No. Y, pp.xxx–xxx.

Biographical notes: Naveen Shetty is a PhD student at the Department of Civil Engineering at KU Leuven, Belgium. He obtained his Master in Structural Engineering from Bauhaus University Weimar, Germany. His research focuses on fracture characterisation of masonry under compression using different NDT methods and numerical modelling. He has spent a three months research stay at Universitat Politècnica de Catalunya (UPC), Barcelona in the framework of micro-modelling of masonry.

Georgios Livitsanos is a PhD student at the Department of Mechanics of Materials and Constructions at Vrije Universiteit of Brussels, Belgium. He obtained his Master in Civil Engineering from the University of Patras, Greece. His research focuses on elastic wave propagation in layered brittle materials based on combined NDT methods. He has spent a two months research stay at the Technical University of Milan, Italy in the framework of monitoring slender masonry structures.

Els Verstrynge is an Assistant Professor at the Civil Engineering Department at KU Leuven, and Guest Professor at the Raymond Lemaire International Centre for Conservation in Leuven, Belgium. She has a background in Structural and Architectural Engineering. Her research focuses on 'Multiscale analysis of damage and degradation in building materials and existing/historic structures'. She is active in several international networks for advanced non-destructive testing and assessment of heritage structures and she is involved in renovation projects dealing with monitoring, reliability assessment and strengthening of structures.

Dimitrios G. Aggelis is a Professor at the Department of Mechanics of Materials and Constructions at the Vrije Universiteit of Brussels, Belgium. His main area of interest includes characterisation of cementitious materials, expanding also to composites and metals by use of non-destructive inspection techniques focused on elastic wave propagation. He is active member of several technical committees of Rilem and was the L'Hermite medalist of 2012.

Danny Van Hemelrijck is a Professor and Head of the Department of Mechanics of Materials and Constructions at the Vrije Universiteit of Brussels, Belgium. He is a member of different scientific organisations, mainly the 'National Committee of Theoretical and Applied Mechanics' (adjunct-secretary), the 'European Society of Composite Materials (ESCM)' (member of the council) and the 'European Society of Experimental Mechanics (EuraSEM)' (member of the executive council as permanent secretary).

Koen Van Balen is a Professor at the Civil Engineering Department at KU Leuven. He carries out research and teaches on binders, masonry and sustainable construction methods. He is the Director of the Raymond Lemaire International Centre for Conservation (RLICC) at the University of Leuven. He is the holder of the UNESCO Chair on preventive conservation, monitoring and maintenance of monuments.

Martine Wevers is a Professor and chair of the Department of Materials Engineering at KU Leuven. She is coordinating the research group 'Materials performance and non-destructive evaluation' at the Department of Materials Engineering. She is responsible for the NDT research and the research on the mechanical behaviour of materials. She is specialised in the in-situ or online damage monitoring techniques (acoustic emission, optical fibres and sensors for structural health monitoring) and the evaluation of microstructural damage in materials using X-ray computed tomography.

This paper is a revised and expanded version of a paper entitled 'Visualization of crack propagation in brick masonry couplets under compression' presented at 10th International Masonry Conference, Milan, Italy, 9–11 July 2018.

1 Introduction

Masonry is a brittle composite material consisting of bricks and mortar with different mechanical properties, such as stiffness and strength. Such combination of bricks and mortar subjected to compression leads to a complex distribution of stress and strain between the brick units and mortar joints (Kaushik et al., 2007; Gumaste et al., 2007; Ravula and Subramaniam, 2016). For this reason, numerous research studies have focused on interpreting the failure modes in masonry under compression.

Typically, most studies have focused on masonry consisting of stiffer bricks and relatively soft mortar. Hilsdorf (1969) made the first attempt to propose a theory in which the masonry failure is governed by the strength of the mortar as described by the Mohr's Coulomb criterion. During compression of such masonry prisms, Hilsdorf (1969) reported the observation of triaxial compression in mortar and axial compression coupled with bilateral tension in bricks. However, this failure theory has been developed based on the elastic behaviour in brick and mortar. Khoo and Hendry (1973) used a maximum lateral strain criterion for the brick as the limiting failure state. Whereas, the theory

proposed by Atkinson and Noland (1983) included force equilibrium and strain compatibility requirements that accounted for nonlinear behaviour of mortar. Therefore, this failure theory differs from previous failure theories (Hilsdorf, 1969; Khoo and Hendry, 1973) because the effects of the nonlinear behaviour of mortar was not included. Based on an experimental and analytical study, McNary and Abrams (1985) evaluated and validated the failure criteria of masonry prisms, which considers the nonlinear (softening) behaviour of mortar. It was shown that the tensile splitting of masonry units was induced by the lateral expansion of the confined mortar. Khoo and Hendry (1973), Atkinson and Noland (1983) and McNary and Abrams (1985) concluded that the most significant parameter for the masonry failure under compression is the nonlinear deformational properties of the mortar. This last observation has also been confirmed in analytical context in Drougkas et al. (2019).

In this context, Hayen et al. (2005) performed a number of triaxial compressive tests on cement and lime-based mortar types with the aim to understand the mechanical behaviour of mortar under a triaxial stress state. For lime mortars having lower Young's modulus than the bricks, the change from brittle to a combined elastic and plastic behaviour with pore collapse mechanism upon triaxial compressive loading conditions was evidenced.

On contrast, very few investigations have been carried on the compressive behaviour of soft bricks coupled with stiffer mortar. However, the available literature (Kaushik et al., 2007; Gumaste et al., 2007; Ravula and Subramaniam, 2016) indicates that such masonry types consist of triaxial compression in bricks and axial compression with lateral tension in mortar joints.

According to all these theories (Kaushik et al., 2007; Gumaste et al., 2007; Ravula and Subramaniam, 2016; Hilsdorf, 1969; Khoo and Hendry, 1973; Atkinson and Noland, 1983; McNary and Abrams, 1985; Drougkas et al., 2019), different failure mechanisms in masonry are possible based on the relative elastic properties of brick and mortar components, such as:

- If the brick's stiffness is higher than the mortar's stiffness, the mortar will be under triaxial compression and the bricks will be under uniaxial compression and bilateral tension. Hence, the failure of masonry is initiated by the tensile splitting of the brick [see Figure 1(a)].
- If the brick's stiffness is lower than the mortar's stiffness, the bricks will be under triaxial compression and the mortar will be under uniaxial compression and bilateral tension. Hence, the failure of masonry is initiated by the tensile splitting of the mortar [see Figure 1(b)].
- If the brick's stiffness is comparable with mortar's stiffness, a more homogeneous behaviour is expected, with possibly the formation of conical shear planes due to deformation constraints between the test apparatus (loading plate) and the specimen.

The model depicted in Figure 1 indicates the formation of tensile cracks under uniaxial compression which propagate into macro cracks, but to confirm the theories on failure mechanisms from other researchers (Kaushik et al., 2007; Gumaste et al., 2007; Ravula and Subramaniam, 2016; Hilsdorf, 1969; Khoo and Hendry, 1973; Atkinson and Noland, 1983; McNary and Abrams, 1985; Drougkas et al., 2019), the visualisation of crack initiation at micro scale is necessary. Since the lateral expansion is as well governed by the Poisson's ratio, it also has an effect on the brick-mortar interaction. However, since

the constant Poisson's ratio is only valid in the elastic range and difficult to quantify accurately for the small-scale specimens experimentally, it will not be explicitly investigated here. The main objective of the experimental test herein presented is to visually examine the crack initiation in masonry specimens of different mortar types under compression. The crack initiation and propagation in masonry is assessed through thickness by using X-ray micro-CT and on the surface with digital image correlation (DIC). Micro-CT images and DIC strain maps are compared to validate the crack initiation and propagation in masonry under compressive loading.

Figure 1 Schematic representation of stress state and crack initiation in (a) stiff brick coupled with soft mortar ($E_b > E_m$) (b) soft brick coupled with stiff mortar ($E_b < E_m$)

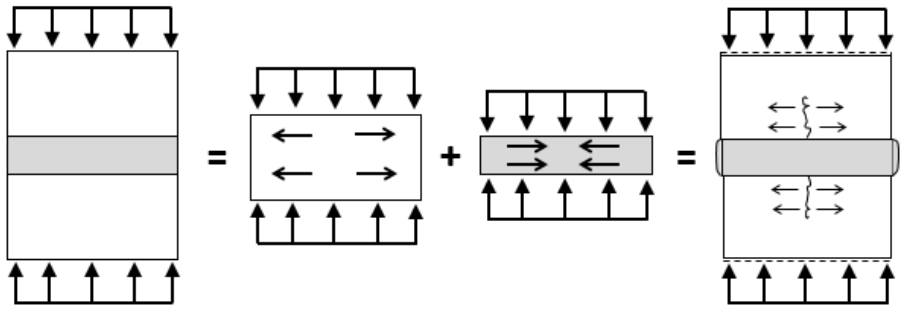

(a)

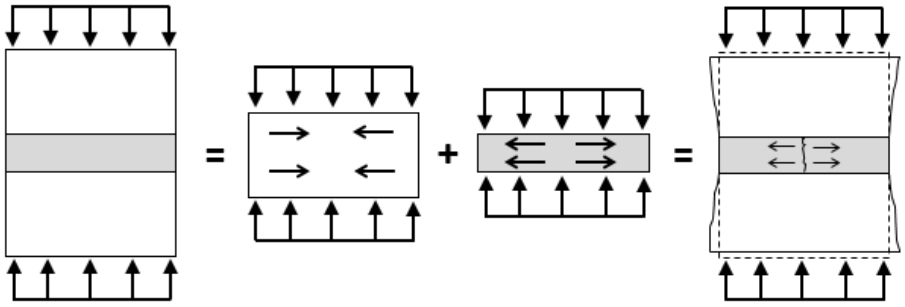

(b)

2 Techniques for crack observation

X-ray computed tomography allows to visualise the inner structure of a non-transparent specimen, based on the attenuation of X-rays (Wevers et al., 2001). In the past, micro-CT has been used at the Department of Civil Engineering at KU Leuven to study small masonry samples. The failure mechanism of brick masonry with cement and lime mortars under compressive loading was investigated by Hendrickx et al. (2010) on an X-ray AEA Tomohawk CT system combined with a mechanical press. In their study, four types of mortar were selected, and one of those had two different curing procedures, which brings the total to five (cement mortar, hybrid lime-cement mortar, hydraulic lime mortar,

non-carbonated lime hydrate mortar and carbonated lime hydrate mortar). For detailed properties of the mortar and test setup, the reader is referred to Hendrickx et al. (2010).

Figure 2 Vertical and horizontal section of each brick-mortar type for crack visualisation after failure of the specimen (see online version for colours)

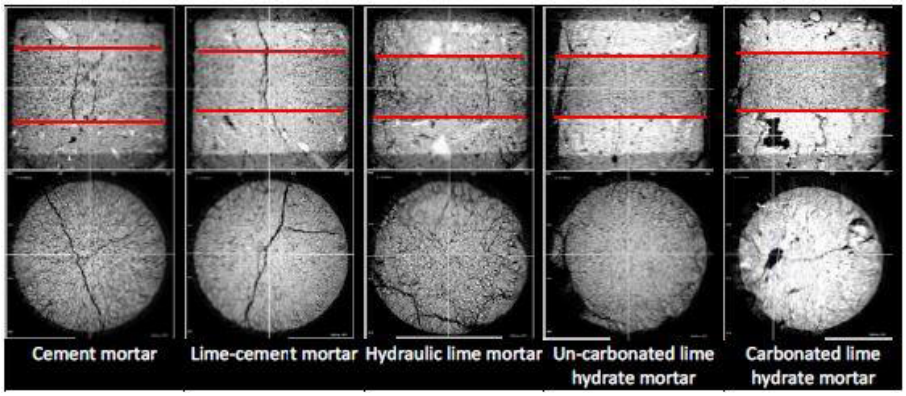

Note: Red lines indicate brick-mortar interface

Source: Hayen et al. (2005)

Table 1 Summary of the applied strain measurement techniques from the literature

Reference	*Mortar type*	*Dimensions of masonry sample*	*Strain measurement technique*	*Gauge length*
Kaushik et al. (2007)	Cement	230 × 110 × 400 mm^3	Extensometers	200 ± 12 mm
	Lime-cement			25 ± 5 mm
Gumaste et al. (2007)	Cement	230 × 105 × 460 mm^3	Demountable mechanical strain gauge (DEMEC)	200 mm
	Lime-cement	600 × 105 × 520 mm^3		
		665 × 230 × 520 mm^3		
Ravula and Subramaniam (2016)	Cement	220 × 100 × 400 mm^3	Digital image correlation (DIC)	-
			Linear variable differential transformer (LVDT)	160 mm
Drougkas et al. (2016)	Air lime	290 × 140 × 290 mm^3	Linear variable differential transformer (LVDT)	100 mm
	Hydraulic lime			
Segura et al. (2018)	Hydraulic lime	639 × 148 × 658 mm^3	Linear variable differential transformer (LVDT)	100 mm
		312 × 148 × 288 mm^3		
Livitsanos et al. (2018)	Hydraulic lime	194 × 110 × 60 mm^3	Digital image correlation (DIC)	-

The scan images in Figure 2 show the vertical and horizontal section of each brick-mortar type after the final loading step. Only macro cracks were visible from the resolution of these images (45.6 μm/pixel). In addition, the slight movement of the plates of the press during scanning might have caused a loss of sharpness in the images. It

should be noted that the experimental study (Hendrickx et al., 2010) has been performed with a conventional CT system. Hence, in this study, a high-resolution micro-CT technique with powerful source of X-rays is applied to visualise the internal structure of the masonry and its failure mechanism on a micro scale level during the subsequent load steps.

A wide range of experimental techniques has been applied in the literature, including local strain measurements and visualisation techniques, as summarised in Table 1. The application of different techniques has indicatively confirmed the general observation of local failure mechanisms (Kaushik et al., 2007; Gumaste et al., 2007; Ravula and Subramaniam, 2016; Drougkas et al., 2016; Segura et al., 2018; Livitsanos et al., 2018). However, micro-CT is a more accurate visualisation method for examining the onset of fracture in the internal structure of the masonry in 3D. This paper aims to highlight this current approach while comparing it with DIC, which is able to capture strains on the surface of the specimen.

3 Experimental program

3.1 Materials

A ceramic red clay brick with dimensions 188 × 88 × 63 mm^3 having an average compressive strength of 11.8 N/mm^2 (standard deviation SD = 2.41 N/mm^2) and average Young's modulus of 1,238 N/mm^2 (SD = 208 N/mm^2) was used. For the mortar, the applied sand is a purified fine quartz sand of grading 0/2 from Lommel (Belgium). In this study, four different mortar types were chosen. The mortar composition is given in Table 2. Mortars are prepared using a Hobart planetary mixer at low speed. All components are added subsequently before mixing: first the water, then half of the fine aggregates, all of the binder, and the other half of the fine aggregates.

Table 2 Mortar composition in mass percentage

	Cement[1]	*Lime-cement*[2]	*Hydraulic lime*[3]	*Non-hydraulic lime*[4]
Sand	68%	70%	69%	74%
Binder	17%	15%	15%	9%
Water	15%	15%	16%	17%

Notes: [1]The binder for the preparation of cement mortar is Portland cement, CEM1 42.5R
[2]The binder for the preparation of hybrid lime-cement mortar is mixture of 66.7 mass-% of calcic lime [CL90S] and 33.3 mass-% of cement [CEM1 42.5R]
[3]The binder for the preparation of this lime mortar is hydraulic lime, NHL5
[4]The binder for the preparation of this lime mortar is calcic lime, CL90S

3.2 Small-scale couplets

The preparation of small-scale masonry couplets is an elaborate process, see Figure 3. At the first step, cylindrical samples with a diameter of 30 mm and height of 18 mm were cored from the brick. All samples were oven-dried at 50°C and immersed in water for 2 seconds before application of mortar. In the second step, a fabrication plate with three screws arranged in a circular pattern was prepared to simplify the preparation of couplets. The lower piece of the brick is positioned on the plate and the screws are tightened to fix

the position. An excess of mortar is then applied, and the top piece of the brick is brought in contact with the mortar and firmly pressed. The mortar thickness is 12 mm, which brings the total height of the couplet to 48 mm approximately. In the next step, the screws are loosened, and the sample is taken out from the fabrication plate. A thin layer of mortar is placed on top and bottom of the samples, and slightly pressed under the platens of the mechanical press to make it a flat surface for an equal distribution of load. During the test, a thin layer of Teflon sheet was placed on top and bottom of the sample to avoid frictional activities. Lastly, a flat spatula is used to give a smooth finishing for the joint. The samples are stored at 20°C and 65% relative humidity.

Figure 3 (a) Cylindrical sample cored from the brick (b) Fabrication plate (c) Preparation of small-scale couplet (d) Test sample (see online version for colours)

(a) (b) (c) (d)

Figure 4(a) shows the details and dimensions of the small-scale masonry couplet. For each type of masonry, two samples were prepared and tested after 28 days (i.e., 2*4 = 8 tests in total) to maintain universality among all the mortar types. However, that the curing time of 28 days is too low for lime mortar, and therefore, the mortar showed even lower strength and stiffness during testing than it would at the age of several months. One representative sample for each type of masonry has been discussed further in this paper. On average, the specifications of the representative masonry samples are: diameter = 30 mm, height = 48 mm, mass = 59 g. The objective of choosing such small sample size is to achieve high resolution of the scan images.

3.3 Full-scale couplets

In addition to the small-scale couplets, required for X-ray CT, full-scale couplets were constructed as well, to avoid that shape and size effects on the crack initiation and propagation in small samples would affect the conclusions of this research. The masonry couplets were built with two full bricks bonded together by a mortar joint. All bricks were immersed in water for 2 seconds before application of mortar. The indentation of the brick was filled with mortar and the top brick was pressed into the mortar joint. The surplus of mortar squeezing outwards was scrapped out for later completion. A level metre was used to check the vertical and horizontal alignment of the brick. The thickness of the mortar joints was approximately 12 mm. After brick laying, the joints were finished and brushed to make them slightly rough and level with the brick surface. A thin layer of gypsum is placed on top and bottom of the couplet and slightly pressed under the platens of the hydraulic press to make it a flat surface for an equal distribution of load. Figure 4(b) shows the details and dimensions of the full-scale masonry couplet. On average, the couplet dimensions were approximately 188 × 88 × 138 mm^3. For each type

of masonry, three samples were prepared and tested after 28 days (i.e., 3*4 = 12 tests in total).

Figure 4 Details and dimensions of (a) small-scale masonry couplet and (b) full-scale masonry couplet

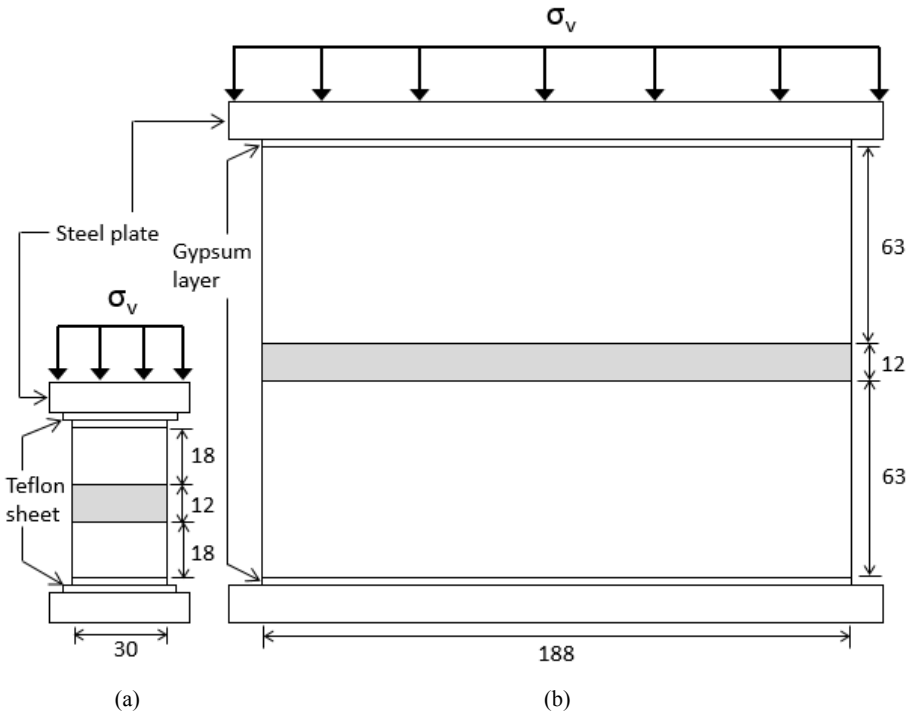

4 Testing procedure

4.1 Micro-CT

The X-ray CT scans were carried out at the Department of Materials Engineering at KU Leuven on a 'Phoenix Nanotom S(GE)' system which is capable of covering a resolution of 500 nm up to 50 µm or more [Figure 5(a)]. In medical CT scanners, the X-ray component which carries source and detector is continuously rotated around the object to obtain tomographic images. In the applied X-ray CT, the object rotates, while the X-ray source and the detector remain stationary. Scanning parameters and resolution can be adjusted by moving the axis of rotation supporting the object either closer to the source or to the detector. Additionally, the image resolution is related to the sample size. The applied X-ray detector has a grey scale resolution of 12 bit, 5 megapixels and field of view of 120 × 120 mm^2.

Many factors influence the resolution and sharpness of micro-CT images. Hence, test scans were performed to optimise the setup by adjusting the position of the sample between the source and the detector, and by increasing or decreasing the current and

voltage. After the initial test scans, the source and acquisition parameters mentioned in Table 3 were chosen for all the sample types to achieve high resolution images.

Table 3 Scanning parameters.

X-ray source parameters		*Acquisition parameters*	
Voltage	100 kV	Exposure time	500 ms
Current	260 µA	Voxel size	16.6 µm
Filter	0.1 mm Cu	Spot size	3.1
Target	Tungsten	Rotation angle	0.15º

During scanning, the compressive load needs to be maintained within the sample. Hence, a transparent compression cell was designed and fabricated with polycarbonate, as shown in Figure 5(b). The steel cap of the compression cell is brought in contact with the sample and it compresses the sample upon load application from a mechanical press. At target load levels, the position of the cap is fixed.

An initial scan is made for each undamaged sample placed in the compression cell. A preload of 0.1 kN is applied with a mechanical press and the steel cap is fixed. Then the cell is placed in the sample chamber of the applied micro-CT equipment, and the scans are made while the cell rotates with rotation steps of 0.15º around its vertical axis. The steel cap positioned on top of the masonry sample caused bright streaks in the micro-CT images namely 'streak artefacts' due to the density difference between the steel and the masonry. Hence, a 0.1 mm Cu filter was placed in front of the source to reduce artefacts. The central portion of the sample with a height of 42 mm was scanned as the main region of interest. The scans were made at a resolution of 16 µm/pixel. Each scan takes approximately 1.5 h, generating 2,400 images over a rotation of 360º.

Figure 5 (a) Nanotom equipment (b) View of the compression cell (see online version for colours)

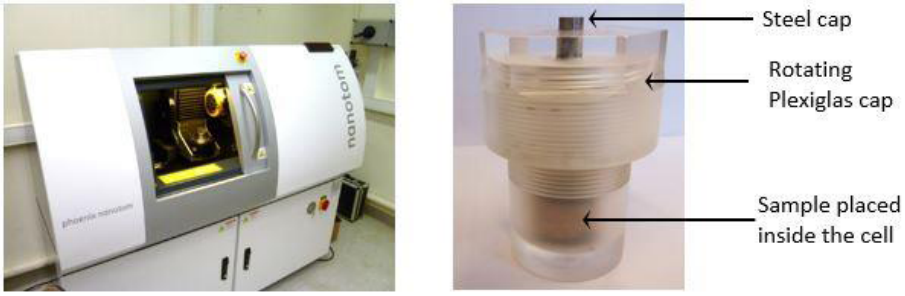

(a) (b)

In the next step, a compressive load was applied at a rate of 0.2 mm/min with a mechanical press until a target stress level or until a sudden drop or change in the force was observed on the digital output of the mechanical press. Load and displacement data were continuously recorded by a digital data acquisition system. The cap of the compressive cell was fixed to maintain the load within the sample and a second scan was performed. During scanning, the stress relaxation in the sample was not able to be recorded due to limitations in the test setup. This procedure was repeated several times

until the sample was extensively damaged. The aim was to perform 8 scans for each sample, resulting in a total test duration of at least 12 h. A similar test setup and procedure has been reported on sandstone by using a SkyScan system (Verstrynge et al., 2014).

4.2 Digital image correlation

DIC is an optical method for determining strains based on a speckle pattern in undeformed and deformed state. The front face of the full-scale couplets was prepared for DIC by coating it with a grey mural paint and applying a black speckle pattern. As the reliability of the DIC maps depends on the speckle size, care should be taken that the speckle size should not be too small nor too large (Sutton et al., 2009; Mojsilovic and Salamanpour, 2016).

Two CCD cameras (Allied Vision Stingray F-504 B/C Fire wire) with a resolution of 2,452 × 2,056 pixels mounted on a tripod were positioned vertically in front of the specimen and both cameras were plugged into the computer. The cameras were fitted with lenses having a focal length of 12 mm (Kowa CCTV LM12JC1MS) and were placed at a distance of 1,500 mm from the specimen surface, as depicted in Figure 6. The light intensity was assured across the surface of the specimen using a pair of halogen lamps. Prior to the actual measurements, calibration was performed by capturing multiple images from the preloaded condition of the specimen to ensure the accuracy of the strain measurement. The correlation process and post processing were conducted by applying Match ID software. During the test, experimental noises were evaluated by assessing the difference in grey level between two subsequent images from each loading position. For this setup, the standard deviation of the error on the horizontal and vertical displacement was found to be equal to 0.0325 mm and 0.0256 mm respectively.

Figure 6 Schematic representation of experimental setup for DIC measurements (side view) (see online version for colours)

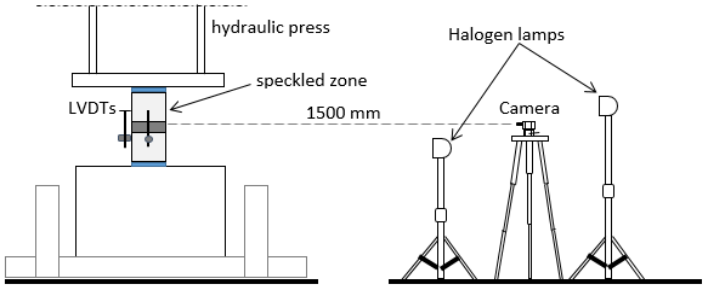

In this work, a subset-based method is applied to correlate two speckle patterns. A subset size equal to 18 × 18 pixels was used for the correlation. During analysis, the zero-normalised sum of squared differences (ZNSSD) correlation is adopted in combination with a bicubic spline subpixel interpolation scheme (Sutton et al., 2009). This scheme accounts for offset and scaling in intensity variations and takes into account the lightning differences between the two cameras. Although several kinds of shape functions are available (Sutton et al., 2009), affine shape function is used as it allows the subset to shear, stretch, rotate and translate.

Cyclic compression tests were performed on the masonry couplets using a hydraulic testing machine 'Instron' with a maximum capacity of 2,500 kN. The applied loading rate was 0.25 kN/s. Up to six loading-unloading cycles with increasing peak load were targeted for each test. Vertical deformation of the couplet was measured at backside and either sides of the couplet with three LVDTs, with a peak displacement range of ±2.5 mm and 0.1% accuracy.

5 Results and discussion

5.1 Compression tests on constituent materials

Initially, the difference in elastic properties of the component materials should be determined. Hence, compression tests on brick and mortar cubes with standard dimensions equal to 40 × 40 × 40 mm^3 were performed. Five tests were performed for each material. A thin layer of Teflon sheet was placed on the top and bottom surfaces of the brick and mortar cubes. The vertical deformation of the cubes was recorded using three surface mounted LVDTs at the centre and opposite faces of the cubes. Figure 7 presents the compressive stress-strain curves for the bricks and mortar types.

Figure 7 Stress-strain curves from compression tests, (a) brick cubes (b) cement mortar (c) lime-cement mortar (d) hydraulic lime mortar (e) non-hydraulic lime mortar cubes (see online version for colours)

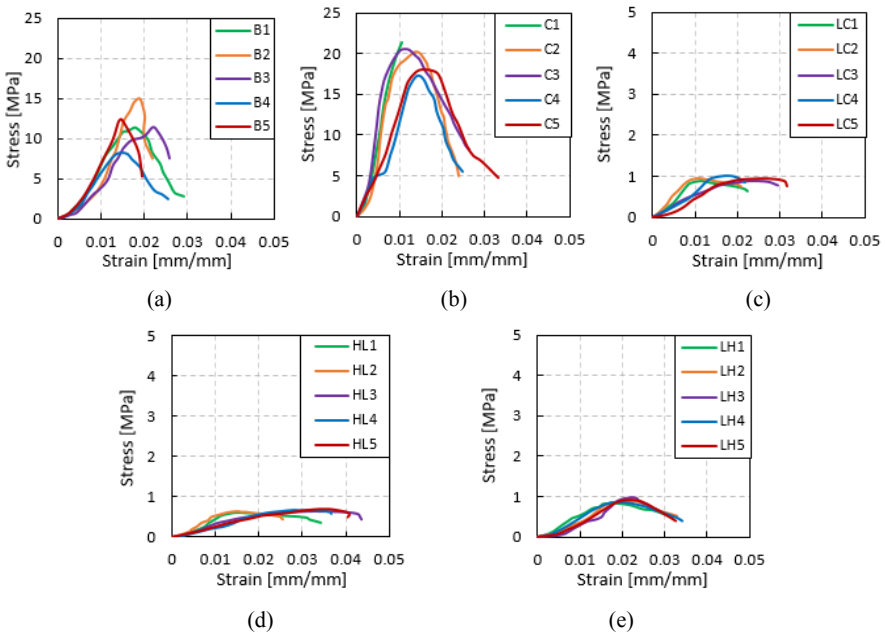

From the stress-strain curves, the modulus of elasticity (E_b, E_m) was calculated by measuring the slope of the secant modulus between 20% and 60% of the ultimate strength of the specimens. A summary of the results showing the average values of compressive strength (f_b, f_m) and modulus of elasticity (E_b, E_m) is given in Table 4. As can be seen from Table 4, the cement mortar (f_m = 19.58 N/mm^2, E_m = 1,900 N/mm^2) is stronger and stiffer than the brick. In the other cases, the brick (f_b = 11.80 N/mm^2, E_b = 1,238 N/mm^2) is stronger and stiffer than the lime-based mortars. For all the specimens, the failure was due to the formation of vertical splitting cracks in the middle with a cone at the ends.

Table 4 Mechanical properties of brick and mortar

Brick type	*Number of samples*	*Compressive strength 'f_b' [N/mm^2]*	*Elastic modulus 'E_b' [N/mm^2]*
Red clay brick (B)	5	11.80 (2.41)	1,238 (208)
Mortar type	*Number of samples*	*Compressive strength 'f_m' [N/mm^2]*	*Elastic modulus 'E_m' [N/mm^2]*
Cement (C)	5	19.58 (1.84)	1,900 (445)
Lime-cement (LC)	5	1.04 (0.10)	166 (25)
Hydraulic lime (HL)	5	0.63 (0.03)	67 (10)
Non-hydraulic lime (LH)	5	0.98 (0.04)	103 (19)

Note: Values are indicated with average (standard deviation)

5.2 Compression tests on masonry couplets

This section presents the results of the experimental test on masonry couplets as explained in Sections 3 and 4. Representative stress-strain curves are presented in Figure 8(a), Figure 8(b), Figure 9(a) and Figure 9(b) for four different types of masonry samples which were tested with X-ray micro-CT. Scan moments are indicated on the stress-strain graphs. Figure 8(a1) to Figure 8(b3), Figure 9(a1) to Figure 9(b3) show a vertical slice image of the samples at subsequent stress levels.

In general, from the scan images, the following observations can be made. The void space around the sample in the compression cell, as well as the pores in the sample appear nearly black as they correspond to low density phases. The grains in the sample appear nearly white as they correspond to high density phases. The distinction between the brick and mortar can be clearly made. At mid-section of the sample, the grains in the mortar are densely packed compared to the bricks. A good bonding of the brick-mortar interface can be observed. The crack initiation and propagation observed from the scan images from Figures 8 and 9 are detailed in Table 5.

Similar results were obtained for the other samples that are not pictured in this paper. Micro-CT results successfully indicated the crack initiation and propagation in small-scale couplets. However, it is equally important to know whether similar crack progress is witnessed in the full-scale couplets to rule out scaling effects. To address this, DIC was applied to have a full 2D strain-based investigation of damage progress on the surface of the couplets.

Figure 8 Results of X-ray micro-CT: stress-strain graph of (a) red brick with cement mortar (a1) scan 1 at 0 MPa (a2) scan 5 at 0.93 MPa (a3) scan 8 at 2 MPa, (b) red brick with lime-cement mortar (b1) scan 1 at 0 MPa (b2) scan 5 at 1.47 MPa (b3) scan 8 at 1.88 MPa (see online version for colours)

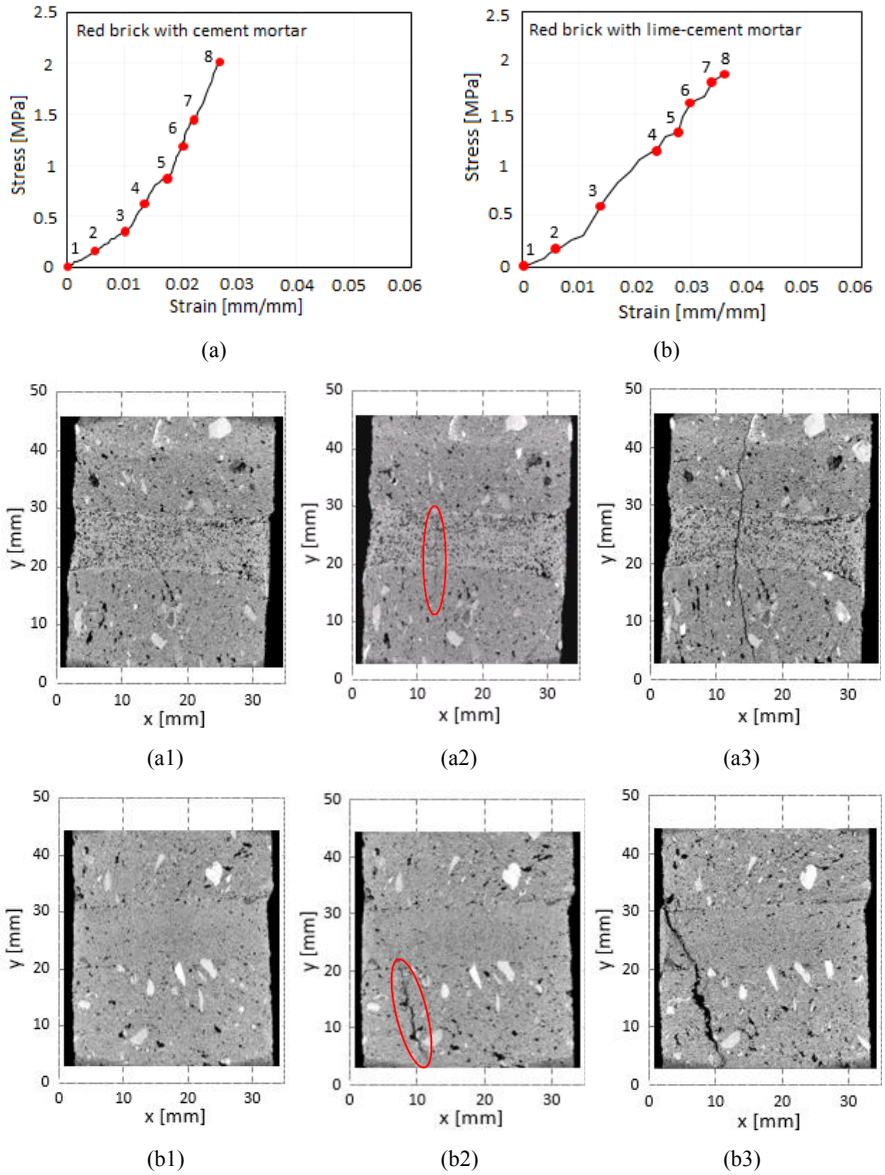

Notes: Vertical slices obtained by X-ray micro-CT on a red brick with cement mortar (a1–a3) and red brick with lime-cement mortar (b1–b3) sample. Scan moments are indicated on the stress-strain graphs.

Figure 9 Results of X-ray micro-CT: stress-strain graph of (a) red brick with hydraulic lime mortar (a1) scan 1 at 0 MPa (a2) scan 6 at 0.98 MPa (a3) scan 8 at 1.6 MPa, (b) red brick with non-hydraulic lime mortar sample (b1) scan 1 at 0 MPa (b2) scan 6 at 1.25 MPa (b3) scan 8 at 1.8 MPa (see online version for colours)

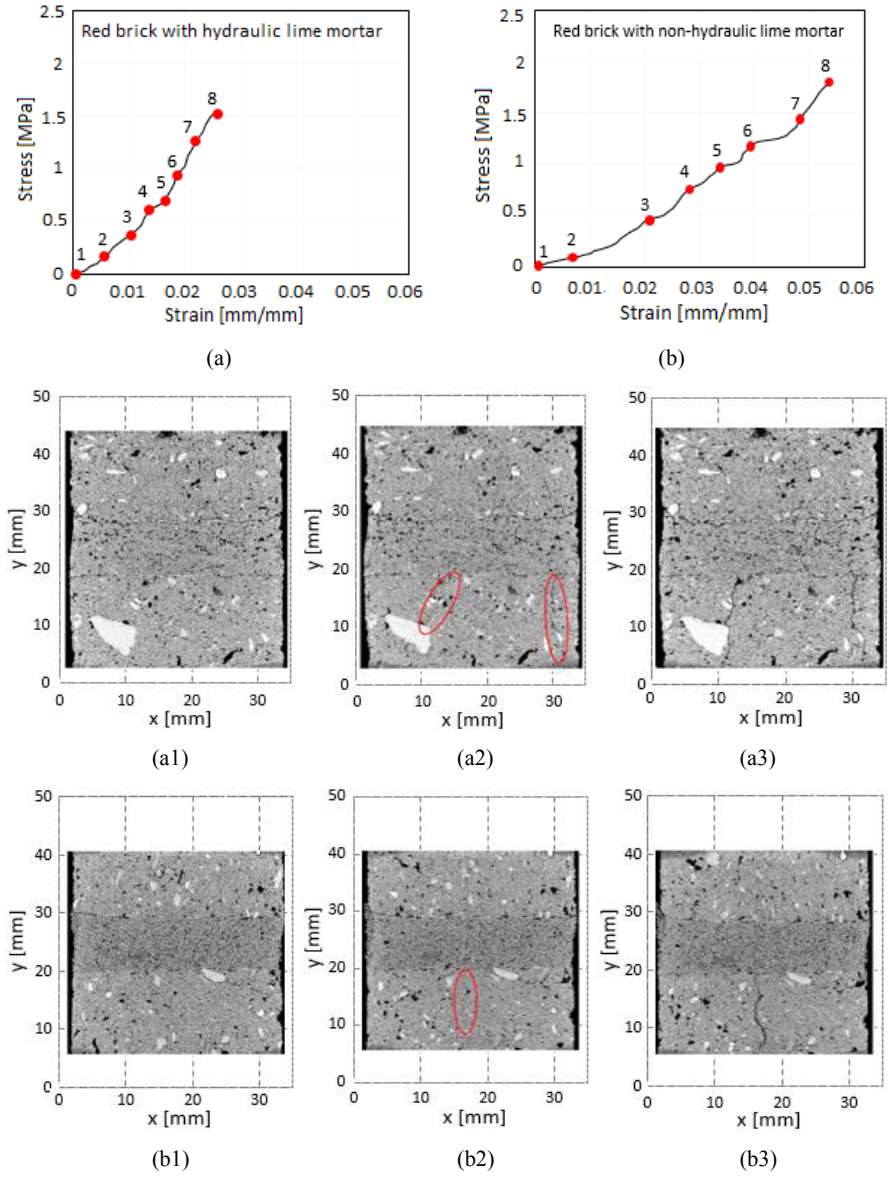

Notes: Vertical slices obtained by X-ray micro-CT on a red brick with hydraulic lime mortar (a1-a3) and red brick with non-hydraulic lime mortar (b1-b3) sample. Scan moments are indicated on the stress-strain graphs.

Figure 10 Results of DIC: stress-strain graph of (a) red brick with cement mortar (a1) DIC at 2.1 MPa (a2) DIC at 3.91 MPa (a3) DIC at 5.78 MPa, (b) red brick with hydraulic lime mortar (b1) DIC at 2.71MPa (b2) DIC at 3.56 MPa (b3) DIC at 4.14 MPa (see online version for colours)

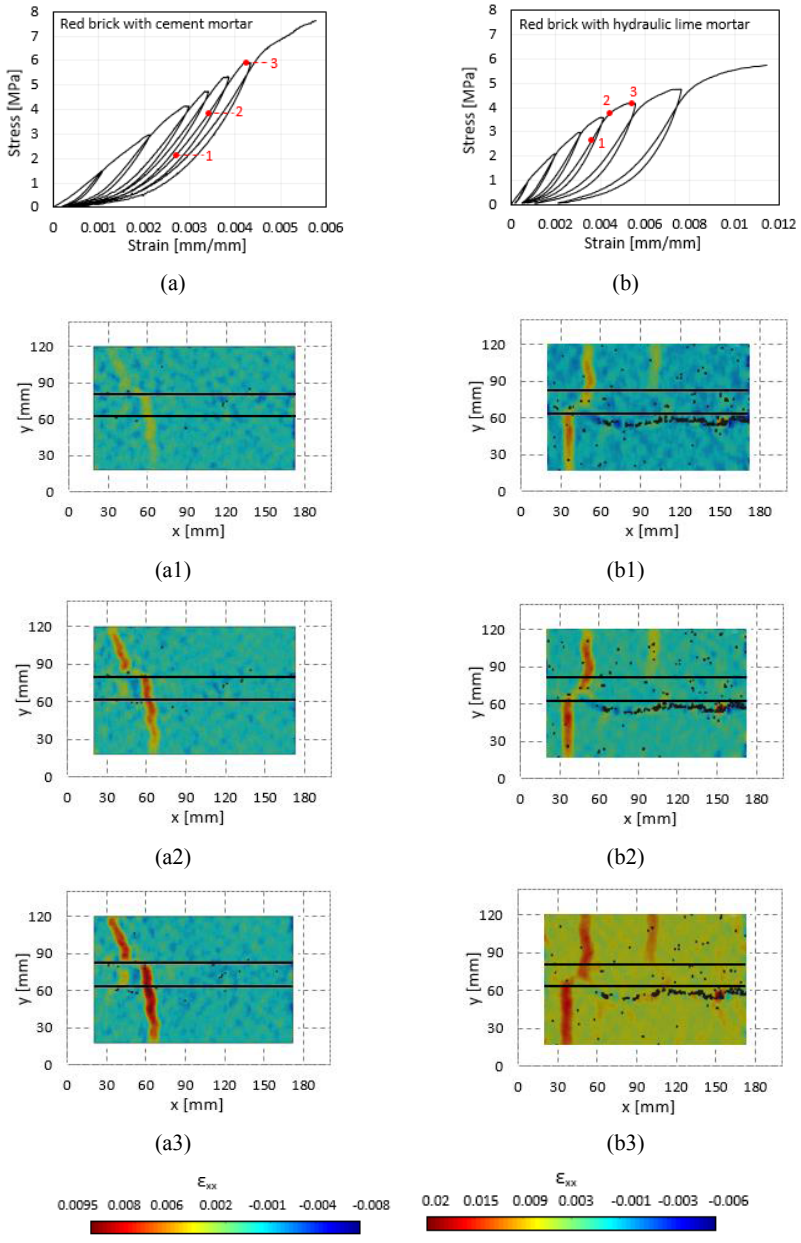

Notes: DIC maps of horizontal strain 'ε_{xx}' on a red brick with cement mortar (a1–a3) and red brick with hydraulic lime mortar (b1–b3) sample. DIC moments are indicated on the stress-strain graphs.

Figure 11 Lateral strain distribution in mortar and bricks for (a) clay brick with cement mortar and (b) clay brick with hydraulic lime mortar (see online version for colours)

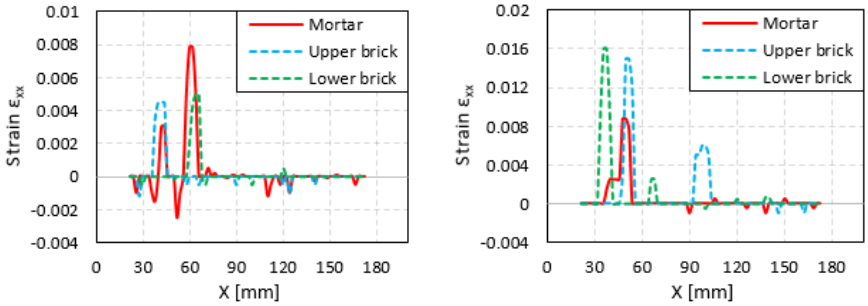

Table 5 Overview of the results explained from the visualisation of X-ray micro-CT images

Masonry type	*Observation*
Clay brick with cement mortar	A tensile crack appears to be generated in the mortar joint [Figure 8(a2)]. The crack in the joint continued to propagate into the brick at both sides at an increasing stress level [Figure 8(a3)].
Clay brick with lime-cement mortar	A tensile-shear crack originates in the brick, near the location of two larger pores [Figure 8(b2)]. The crack propagates into the joint at an increasing stress level [Figure 8(b3)].
Clay brick with hydraulic lime mortar	Two different cracks i.e., an inclined tensile-shear crack and a vertical tensile crack originate at two different locations in the brick independently [Figure 9(a2)]. The cracks continued to propagate downwards in the brick at an increasing stress level [Figure 9(a3)].
Clay brick with non-hydraulic lime mortar	A tensile crack originated at the mid-section of the brick near a pore[Figure 9(b2)]. The crack continued to propagate downwards in the brick and slightly upwards at an increasing stress level [Figure 9(b3)].

In this investigation, two masonry couplets with cement and hydraulic lime mortar are considered for further analysis to confirm the visual output of the micro-CT images. Representative stress-strain curves for the two types of couplets are presented in Figures 10(a) and 10(b). The points in the graph indicates the subsequent stress levels at which the DIC maps are presented. Figures 10(a1) to 10(a3) and Figures 10(b1) to 10(b3) present the 2D-DIC map of the horizontal strain contour 'ε_{xx}' for the two masonry types respectively. The crack initiation and propagation observed from the DIC maps are detailed in Table 6. It should be noticed that the early crack initiation cannot as easily be observed from the DIC results due to the lower resolution of the strain maps (smeared strains on the surface of the specimen), compared to the micro-CT images (discrete cracks, images with a 16 µm pixel size).

The average horizontal strains 'ε_{xx}' are extracted from the three regions of the couplet such as the upper brick, mortar and the lower brick as shown in the Figures 11(a) and 11(b). This analysis was done for clay brick with cement mortar at 3.91 MPa [50% of f_c, Figure 11(a)] and for clay brick with hydraulic lime mortar at 3.56 MPa [60% of f_c, Figure 11(b)].

Table 6 Overview of the results explained from the visualisation of DIC strain maps

Masonry type	*Observation*
Clay brick with cement mortar	A tensile crack appears to be generated in the mortar joint [Figure 10(a1)]. The crack in the joint continued to propagate downwards in the brick at an increasing stress level. At this stage, another crack originates in the brick and propagates upwards [Figure 10(a2)]. Tensile splitting cracks with high strains can be observed in the mortar joint [Figure 10(a3)].
Clay brick with hydraulic lime mortar	Two vertical cracks originate in the upper and lower brick independently [Figure 10(b1)]. The cracks continued to propagate in the brick at an increasing stress level [Figure 10(b2)]. Tensile splitting cracks with high strains can be observed in the bricks [Figure 10(b3)].

In Figure 11(a), for the clay brick with cement mortar, it is observed that vertical splitting cracks occur in the bricks and mortar joint, with higher strains in the joint compared to the bricks. The ultimate failure was produced by major vertical cracks in mortar and bricks, followed by localised crushing of masonry. In Figure 11(b), for the clay brick with hydraulic lime mortar, high strains occur in the brick compared to the mortar. The ultimate failure was produced by vertical splitting of bricks, followed by spalling of the outer layer of the joint and bricks.

Table 7 summarises all findings and illustrates the link between the X-ray micro-CT and DIC results. All experimental results are in agreement with the general theory on crack initiation for different cases of stiffness properties.

Table 7 Comparison of crack initiation from general theory (Figure 1) and observation from micro-CT and DIC results

Models	*Stiffness*	*Location of crack initiation*		
		General theory (Figure 1)	*Micro-CT (sample 1/2)*	*DIC (sample 1)*
Clay brick with cement mortar	$E_b < E_m$	Mortar	Mortar/Mortar	Mortar
Clay brick with lime-cement mortar	$E_b > E_m$	Brick	Brick/Brick	-
Clay brick with hydraulic lime mortar	$E_b > E_m$	Brick	Brick/Brick	Brick
Clay brick with non-hydraulic lime mortar	$E_b > E_m$	Brick	Brick/Brick	-

6 Conclusions

This paper focuses on experimentally investigating the common failure hypothesis for masonry under compression. The X-ray micro-CT technique proved to be an efficient tool to visualise the internal structure of masonry and its failure mechanisms under compression on a micro-scale level. Crack initiation which could not be traced in previous research, was visualised with the current setup. The resolution of the images allowed to visualise small pores and cracks in the samples. In these tests, the challenge was to predict the exact moment of crack initiation for each masonry type. For the masonry with strong mortar, vertical tensile cracks were initiated in the mortar and

propagated into the brick. For the masonry with weak mortar, vertical tensile cracks were initiated in the brick and propagated into the mortar.

Furthermore, DIC applied on full-scale couplets of masonry with cement and hydraulic lime mortar indicated the strains at the different parts of the couplets where the cracks initiated. The magnitude of the strains is attributed to the difference in stiffness of brick and mortar and the location of the crack initiation zone. In conclusion, the observations made from the X-ray micro-CT images and DIC strain maps are in accordance with the general theory on the failure modes of masonry under compression.

Acknowledgements

The Research Fund – Flanders (FWO) is acknowledged for funding the FWO project 'AE- FracMasS: advanced Acoustic Emission analysis for Fracture mode identification in Masonry Structures' (G.0C38.15).

References

Atkinson, R.H. and Noland, J.L. (1983) 'A proposed failure theory for brick masonry in compression', *Proceedings of Third Canadian Masonry Symposium*, Edmonton, pp.5.1–5.17.

Drougkas, A., Roca, P. and Molins, C. (2016) 'Compressive strength and elasticity of pure lime mortar masonry', *Materials and Structures*, Vol. 49, No. 3, pp.983–999.

Drougkas, A., Verstrynge, E., Hayen, R. and Van Balen, K. (2019) 'The confinement of mortar in masonry under compression: Experimental data and micro-mechanical analysis', *International Journal of Solids and Structures*, Vol. 162, pp.105–120.

Gumaste, K.S., Nanjunda Rao, K.S., Venkatarama Reddy, B.V. and Jagadish, K.S. (2007) 'Strength and elasticity of brick masonry prisms and wallettes under compression', *Materials and Structures*, Vol. 40, No. 2, pp.241–253.

Hayen, R., Van Balen, K. and Van Gemert, D. (2005) 'The mechanical behaviour of mortars in triaxial compression', *Proceedings of the 4th International Seminar on Structural Analysis of Historical Constructions*, Padova, pp.611–618.

Hendrickx, R., Buyninckx, K., Schueremans, L., Kerckhofs, G., Verstrynge, E., Wevers, M and Van Balen, K. (2010) 'Observation of the failure mechanism of brick masonry doublets with cement and lime mortars by microfocus X-ray computed tomography', *Proceedings of the 8th International Masonry Conference*, Dresden, 4–7 July, art. nr. 223.

Hilsdorf, H.K. (1969) 'Investigation into the failure mechanisms of brick masonry loaded in axial compression', *Proceedings of International Conference on Masonry Structural Systems*, Gulf Publishing Co., Houston, Texas, pp.34–41.

Kaushik, H.B., Rai, D.C. and Jain, S.K. (2007) 'Stress-strain characteristics of clay brick masonry under uniaxial compression', *Journal of Materials in Civil Engineering*, Vol. 19, No. 9, pp.728–739.

Khoo, C.L. and Hendry, A.W. (1973) 'A failure criteria for brick-work in axial compression', *Proceedings of Third International Brick Conference*, Essen, England, pp.141–145.

Livitsanos, G., Shetty, N., Hündgen, D., Verstrynge, E., Wevers, M., Van Hemelrijck, D. and Aggelis, D.G. (2018) 'Acoustic emission characteristics of fracture modes in masonry materials', *Construction and Building Materials*, Vol. 162, pp.914–922.

McNary, W.S. and Abrams, D.P. (1985) 'Mechanics of masonry in compression', *Journal of Structural Engineering*, Vol. 111, No. 4, pp.857–870.

Mojsilovic, N. and Salamanpour, A.H. (2016) 'Masonry walls subjected to in-plane cyclic loading: application of digital image correlation for deformation field measurement', *International Journal of Masonry Research and Innovation*, Vol. 1, No. 2, pp.165–187.

Ravula, M.B. and Subramaniam, K.V.L. (2016) 'Experimental investigation of compressive failure in masonry brick assemblages made with soft brick', *Materials and Structures*, Vol. 50, p.19, DOI: 10.1617/s11527-016-0926-1.

Segura, J., Pelà, L. and Roca, P. (2018) 'Monotonic and cyclic testing of clay brick and lime mortar masonry in compression', *Construction and Building Materials*, Vol. 193, pp.453–466.

Sutton, M.A., Orteu, J-J. and Schreier, H.W. (2009) *Image Correlation for Shape, Motion and Deformation Measurements – Basic Concepts, Theory and Applications*, Springer, DOI: 10.1007/978-0-387-78747-3.

Verstrynge, E., Adriaens, R., Elsen, J. and Van Balen, K. (2014) 'Multi-scale analysis on the influence of moisture on the mechanical behaviour of ferruginous sandstone', *Construction and Building Materials*, Vol. 54, pp.78–90.

Wevers, M., De Meester, P. and Swennen, R. (2001) 'Microfocus X-ray computer tomography in materials research', *Insight – Non-destructive Testing and Condition Monitoring*, Vol. 43, No. 10, pp.658–663.